Orographic Gravity Waves Close to the Nonhydrostatic Limit of Vertical Propagation

GÜNTHER ZÄNGL

Meteorologisches Institut der Universität München, Munich, Germany

(Manuscript received 20 August 2002, in final form 25 February 2003)

ABSTRACT

Orographic gravity waves excited by a narrow mountain ridge are investigated with the aid of numerical simulations. When the nondimensional mountain half-width Na/U is around 1—N, a, and U being the Brunt–Väisälä frequency, the dimensional half-width, and the ambient wind speed, respectively—only part of the gravity wave spectrum excited by the mountain is able to propagate vertically. In this case, linear theory, as well as numerical simulations with low mountains, show two wind maxima: one at the mountain crest and one in the lee of the mountain. As Na/U is reduced below 1, the wind maximum in the lee weakens and moves farther downstream, and the maximum at the crest intensifies rapidly with decreasing Na/U. Simulations in which a gap with a level axis is embedded in the mountain ridge demonstrate that the wind perturbations along the gap axis are qualitatively similar to those over the adjacent mountain ridge. However, their magnitude is substantially lower, and the tendency to form a wind maximum at the gap center (corresponding to a maximum at the mountaintop) is rather weak.

When the mountain is high enough for nonlinear effects to become important, the flow structure changes substantially. Provided that Na/U is not below 1, there is a range of nondimensional mountain heights where gravity wave breaking establishes a flow structure very similar to that typical for wider mountains, including strong downslope winds in the lee of the mountain and a pressure drag well above the linear value. The results indicate that nonlinearity can shift the primary wind maximum from the mountain crest into the lee. For $Na/U \approx 0.75$, gravity wave breaking no longer occurs, and the wind maximum is reached at the top of the mountain regardless of its height. Along a gap axis, however, there is a tendency for a pronounced wind maximum on the lee side even for narrow mountain ridges. In agreement with the results known for wider mountains, surface friction is found to reduce the wind speed close to the ground, to promote flow separation from the ground over the lee slope of the mountain and to reduce the tendency toward gravity wave breaking. For $Na/U \approx 1$ and moderate surface friction, the formation of rotors becomes possible even for uniform large-scale flow.

1. Introduction

Gravity waves are a ubiquitous feature over mountainous terrain. As is well known from linear theory, stationary monochromatic gravity waves are able to propagate vertically when their horizontal wavelength ranges between approximately $2\pi U/N$ and $2\pi U/f$—U, N, and f being the horizontal wind speed, the Brunt–Väisälä frequency and the Coriolis parameter, respectively. Shorter gravity waves, dominated by nonhydrostatic dynamics, and long inertio-gravity waves decay with height. Gravity waves excited by an isolated mountain are associated with a surface wind maximum over the lee slope when their wavelength spectrum is dominated by vertically propagating wave components (e.g., Queney 1948). For very narrow mountains, however, the wind maximum is located at the mountain peak, and there is an intermediate range of mountain widths that exhibits wind maxima at the peak as well as in the lee. When the atmospheric structure is such that U/N increases significantly with height, there is a range of wavelengths for which vertical propagation is possible only up to a certain threshold height. Under these circumstances, certain wavelengths may become resonant, leading to the well-known trapped lee waves propagating horizontally downstream (e.g., Scorer 1949; Sawyer 1960). Below the wave crests of trapped lee waves, rotors may form when surface friction forces flow separation from the ground (Doyle and Durran 2002).

Since the discovery of the nonlinear gravity wave amplification mechanism by Clark and Peltier (1977) and Peltier and Clark (1979), which is capable of producing downslope windstorms far exceeding the strength predicted by linear theory, a large number of numerical studies has been performed on various aspects of vertically propagating gravity waves. Most of them focused on relatively wide mountains such that $Na/U \gg 1$, a denoting a characteristic length scale of the mountain (usually its half-width in along-stream direction). This criterion ensures that the wave spectrum excited by the mountain is dominated by vertically prop-

Corresponding author address: Dr. Günther Zängl, Meteorologisches Institut der Universität München, Theresienstraße 37, Munich D-80333, Germany.
E-mail: guenther@meteo.physik.uni-muenchen.de

agating components. Exceptions are studies concerned with trapped lee waves (e.g., Durran and Klemp 1982; Shutts 1992; Koffi et al. 2000) and those by Bacmeister and Schoeberl (1989), Xue and Thorpe (1991), Klemp and Durran (1983), and Dudhia (1993). Bacmeister and Schoeberl considered the propagation of low-amplitude waves into the stratosphere and performed a sensitivity experiment with $Na/U = 3$ in order to test the impact of nonhydrostatic wave dispersion. The latter authors conducted simulations with $Na/U = 2$ (Xue and Thorpe), $Na/U = 1$ (Klemp and Durran, Dudhia), and $Na/U = 0.1$ (Dudhia) for the purpose of model validation.

Yet, there appears to be no study considering nonlinear effects on airflow over a mountain with $Na/U \sim 1$. For this parameter range, linear theory predicts a primary wind maximum at the mountain top and a secondary (weaker) maximum in the lee of the mountain (Queney 1948). This is confirmed by observations of airflow over small hills (e.g., Vosper et al. 2002). However, occasional observations in the Alps (Sládkovič and Kanter 1977; M. Hornsteiner 2002, personal communication) indicate that the dominant surface wind maximum can also be located in the lee of such a narrow mountain ridge or at least in the lee of a gap embedded in such a ridge. The amplification of the wind speed achieved in this situation appears to be of the same order as that found for much wider ridges for which the flow is essentially hydrostatic. This raises the question whether nonlinear effects are able to extend the hydrostatic flow structure with a leeside wind maximum to lower values of Na/U. In addition, the sensitivity of the flow structure to small changes of Na/U is an interesting question that has not been addressed previously.

To gain more insight into the airflow over narrow mountain ridges, numerical simulations have been performed with a mesoscale model. Since the available observations of strong leeside winds are biased towards the vicinity of gaps, indicating that gaps favor the occurrence of high wind speeds, gap effects are also investigated in some detail. The standard setup considers uniform flow over a mountain ridge with a gap in the absence of Coriolis force and surface friction. Sensitivity experiments with Coriolis force and surface friction are also conducted. The nondimensional mountain height Nh_0/U, h_0 being the dimensional maximum mountain height, varies between 0.3 and 2.1 so as to compare quasi-linear flow with strongly nonlinear flow. It will be demonstrated that nonlinear effects, in particular gravity wave breaking, indeed extend the hydrostatic flow regime with a leeside wind maximum to smaller mountain widths. This behavior is especially pronounced in the vicinity of gaps. The experiments with surface friction demonstrate that—in contrast to common belief—the formation of rotors is possible even for uniform large-scale flow.

The outline of the paper is as follows. In section 2, the setup of the simulations is described. Section 3 presents the results, and a summary is given in section 4.

2. Model and setup

The numerical simulations are performed with the nonhydrostatic fifth-generation Pennsylvania State University–National Center for Atmospheric Research (PSU–NCAR) Mesoscale Model (MM5). The model uses a terrain-following sigma-coordinate system that is based on a temporally and spatially constant reference state. For details, the reader is referred to the model description (Grell et al. 1995).

Since the MM5 is set up for simulations with real data, a few modifications were necessary in order to adapt it for idealized simulations. Curvature terms and mapping factors were removed from the equations of motion, and the Coriolis parameter f is set to a constant value of either zero or 10^{-4} s^{-1}. The model is run in dry mode, and the only physical parameterization retained for the simulations is a turbulent-kinetic-energy-based parameterization for vertical mixing and, if surface friction is taken into account, for computing the surface momentum fluxes (Gayno 1994; Ballard et al. 1991). The roughness length is set to either 1 or 50 cm in the frictional runs; otherwise, the surface momentum fluxes are set explicitly to zero. In the remainder of this paper, the simulations without surface momentum fluxes will be referred to as frictionless. It is noted that the MM5-built-in option for switching off surface friction is not used because this option also switches off vertical mixing. For horizontal mixing, which is needed to ensure numerical stability, the modified diffusion scheme described in Zängl (2002a) is used. It computes the diffusion truly horizontally rather than along the coordinate surfaces and greatly reduces the numerical errors over steep orography.

The simulations presented in this study are computed on four interactively nested domains having a horizontal resolution of 10.8 km, 3.6 km, 1.2 km and 400 m, respectively. The numbers of grid points are 61×61 for the first three domains and 61×115 for the innermost domain. Interactive nesting means that a nested domain receives its boundary values from the next coarser domain while the coarser domain gets smoothed information from the nest at every time step for the whole overlap area. This ensures that spurious boundary influences are weak at internal model boundaries. Moreover, the more problematic outer model boundaries can be moved sufficiently far away from the mountain without significant computational costs. In the vertical, 39 full-sigma levels are used, corresponding to 38 half-sigma-levels where all variables except for the vertical wind speed are computed. The lowermost half-sigma level, which will be referred to as surface level in the remainder of this paper, is about 25 m above the ground. The vertical resolution ranges from 60 m near the sur-

face to about 700 m near the upper boundary, which is located at 100 hPa. At the upper boundary, a radiation condition is used to prevent spurious reflections of vertically propagating gravity waves. The radiation condition follows the ideas of Klemp and Durran (1983) and has been modified by the author so as to enhance the range of horizontal wavelengths captured by it. In the standard MM5 implementation, this wavelength range is limited to 12 times the grid distance, which is not sufficient for the nested model domains. In the modified version, the longer wave components are interpolated from the coarser model domain(s), ensuring that the whole spectrum of gravity waves is able to radiate upward. A description of this procedure is given in the appendix of Zängl (2002b). It is mentioned that the local computation of the radiation condition is switched off in the innermost model domain since the wavelength range that would be radiated upward in this case (up to 4.8 km) is not able to propagate vertically under the atmospheric conditions chosen for this study (see below). In the innermost model domain, only the interpolation of the radiation condition from the coarser domains is retained. This way, it is achieved that the vertically propagating part of the wave spectrum is radiated upward without applying the radiation condition to vertically decaying wave components.

The orography used for the simulations is a long, north–south-oriented mountain ridge. Its basic shape is given by

$$h_\mu(x) = h_0[1 + (x/L)^2]^{-\mu}. \quad (1)$$

The shape parameter μ is set to 1.5 except for a few sensitivity experiments for which $\mu = 1$ is used. The length-scale parameter L is set to 1.5 km for $\mu = 1.5$ and to 1 km for $\mu = 1$, corresponding to a half-width a of 1.15 and 1 km, respectively. In meridional direction, the mountain ridge has constant height over a distance of 36 km, followed by a 3-km-long cosine-squared-shaped transition zone on either side. The maximum height h_0 ranges between 300 and 2250 m. In the majority of the simulations, a gap is introduced at the center of the mountain ridge by replacing h_0 with

$$h_0^* = h_0 - h_G \cos^2[\pi y/(2l)] \quad (2)$$

if $|y| \leq l$. The gap depth h_G is equal to h_0, and the gap width l is set to 2 km except for the simulations with $h_0 > 2$ km where l had to be increased to 2.6 km for reasons of numerical stability. As an example, a contour plot of this orography is given in Fig. 1 for $\mu = 1.5$ and $h_0 = 1500$ m. Figure 1 also displays the location of the cross sections shown in the subsequent figures. Line RR' is the section through the northern part of the split mountain ridge, and line GG' goes along the gap axis if a gap is present. Otherwise, line GG' goes through the symmetry axis of the ridge.

The large-scale flow condition is a uniform westerly (ridge normal) wind with a constant speed of either $U = 10$ or 15 m s^{-1}. It is prescribed in the whole model domain at initial time and continuously imposed at the outer model boundaries through a relaxation condition. The Brunt–Väisälä frequency N is set to a constant value of 10^{-2} s^{-1}. It follows that the nondimensional mountain height is obtained by dividing the dimensional height by 1000 and 1500, respectively. The corresponding nondimensional half-width Na/U is 1.15 and 0.77, respectively. For the frictionless simulations, zero Coriolis force is assumed. However, a Coriolis parameter of 10^{-4} s^{-1} is used for the frictional simulations because setting up a uniform stationary large-scale flow is difficult without Coriolis force. Since the along-flow Rossby number U/fa ranges between 67 and 130 for the parameters chosen, it is expected that the inclusion of the Coriolis force does not have a significant effect on the flow over the mountain ridge. To ensure that this is also valid for high mountain ridges that may induce substantial upstream blocking, a few frictionless test runs were performed with $f = 10^{-4}$ s^{-1} and compared with the standard runs. These tests confirmed the absence of significant Coriolis effects. All simulations are carried out until $t = 12$ h, corresponding to a nondimensional time $t^* \equiv tU/L$ of 288 in the $U = 10$ m s^{-1} case. It turned

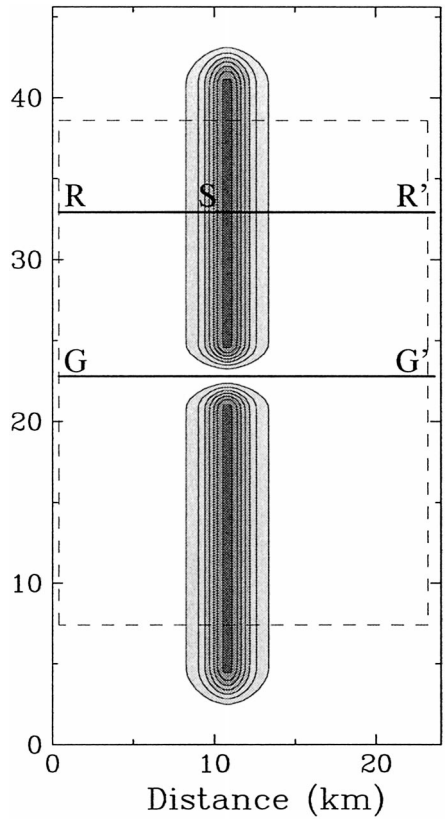

FIG. 1. Orography of the innermost model domain for the mountain ridge with $h_0 = 1500$ m. The contour interval is 200 m, and shading steps are taken every 400 m. The dashed box indicates the subdomain shown in Fig. 10. The solid lines denote the cross sections RR' (ridge) and GG' (gap) shown in the subsequent figures. Section SR' is shown in Fig. 13.

TABLE 1. List of simulations discussed in this paper. The suffix ''r'' denotes simulations using a mountain ridge without a gap. Simulations marked with ''f'' and ''lf'' include Coriolis force and surface friction, the roughness length being 50 cm (1 cm) for ''f'' (lf).

Simulation	h_0 (m)	U (m s^{-1})	Nh_0/U	Na/U	h_0/a
L1, L1r, L1f	300	10	0.3	1.15	0.26
L2, L2r	450	15	0.3	0.77	0.39
N1, N1r, N1f, N1lf	900	10	0.9	1.15	0.78
N2, N2r, N2f, N2lf	1500	10	1.5	1.15	1.31
N3, N3f	2100	10	2.1	1.15	1.83
N4	900	15	0.6	0.77	0.78
N5	1500	15	1.0	0.77	1.31
N6	2100	15	1.4	0.77	1.83
N7	2250	15	1.5	0.77	1.96
S1r	300	10	0.3	1	0.3
S2r	300	15	0.2	0.67	0.3
S3r	300	25	0.12	0.4	0.3
S4r	450	15	0.3	0.67	0.45
Simulations taken from Zängl (2002b)					
W1, W1r	300	10	0.3	30.7	0.01
W2, W2r	900	10	0.9	30.7	0.03
W3, W3r, W3f	1500	10	1.5	30.7	0.05
W4, W4r	2100	10	2.1	30.7	0.07

out that this is well enough to reach a stationary state in all the simulations.

A list of the simulations discussed in this paper is provided in Table 1. The names of the simulations are composed of a capital letter indicating the simulation series, a number, and an optional suffix. Of the leading capital letters, ''L'' (''N'') denotes the simulations covering the linear (nonlinear) parameter range provided that they are conducted with the $\mu = 1.5$ orography. The sensitivity experiments conducted with the standard Witch-of-Agnesi orography (i.e., $\mu = 1$) are named with ''S.'' In addition, Table 1 lists a few simulations already presented in Zängl (2002b). These simulations have been conducted with a much wider mountain ridge ($L = 40$ km or $Na/U \approx 31$) having the same shape as the $\mu = 1.5$ orography (see Zängl 2002b for details). They are named with a ''W'' and are needed for comparison with the results obtained in the present study. The absence of a suffix means that surface friction and the Coriolis force are not taken into account and that the model orography contains a gap. When the name ends with an ''r,'' the orography is a simple ridge without a gap. Finally, ''f'' and ''lf'' indicate the presence of the Coriolis force and of surface friction, the roughness length being 50 cm for f and 1 cm for lf.

3. Results and discussion

The following discussion first considers the flow over the mountain ridge and then the flow along the gap axis. Finally, the experiments with Coriolis force and surface friction are discussed. For the frictionless simulations, Table 2 summarizes the results for the pressure drag and the maximum surface wind perturbation. The pressure drag is normalized by its linear hydrostatic value

$$D_{\text{lin}} = F(\mu)\rho UNh_0^2, \tag{3}$$

TABLE 2. Pressure drag and maximum wind speeds for frictionless simulations. The pressure drag is evaluated along line GG' (see Fig. 1) for the ridge simulations (upper part) along line RR' (see Fig. 1) for the simulations with gap orography (lower part). It is normalized with the linear hydrostatic value given in Eq. (3). Definitions are $u' = (u - U)/U$, $x' = x/L$.

Simulation	Normalized drag	$u'_{\max}$ along RR'	$x'_{\max}$ along RR'	$u_{\max}$ along GG'	$x_{\max}$ along GG'
L1r	0.62	0.129	0.0	0.120	0.0
L2r	0.37	0.298	0.0	0.292	0.0
N1r	1.35	1.076	3.0	1.045	3.2
N2r	0.93	0.923	2.9	0.914	3.4
S1r	0.58	0.153	0.0	0.149	0.0
S2r	0.33	0.205	0.0	0.205	0.0
S3r	0.21	0.248	0.0	0.255	0.0
S4r	0.36	0.333	0.0	0.336	0.0
W1r	1.16	—	—	0.215	0.6
W2r	2.55	—	—	1.396	1.5
W3r	1.99	—	—	1.652	1.4
W4r	1.32	—	—	1.418	1.5
L1	0.58	0.129	0.0	0.028	1.9
L2	0.37	0.311	0.0	0.089	0.0
N1	1.34	1.090	3.2	0.943	3.2
N2	0.95	0.928	2.9	0.974	3.5
N3	0.49	0.799	0.0	0.717	6.2
N4	0.46	0.715	0.0	0.206	0.2
N5	0.63	1.217	0.0	0.347	0.2
N6	0.57	1.143	0.0	0.290	7.7
N7	0.51	0.946	0.0	0.393	7.5
W1	—	—	—	0.093	1.0
W2	—	—	—	1.229	2.8
W3	—	—	—	1.452	1.6
W4	—	—	—	1.574	2.5

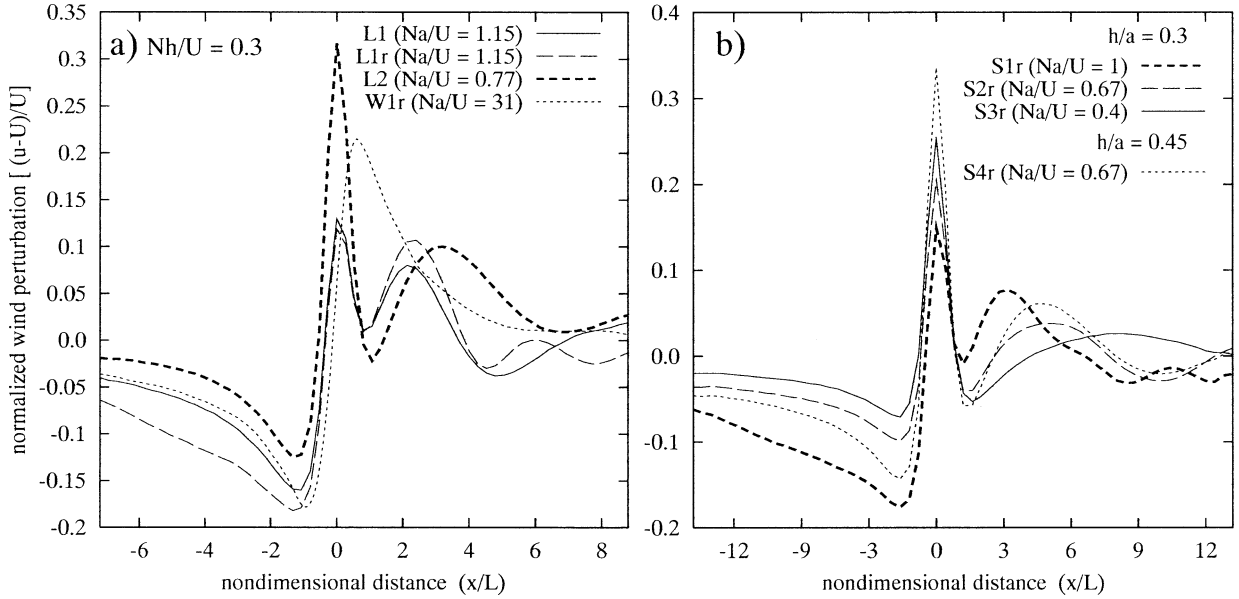

FIG. 2. Normalized surface wind perturbation $u' \equiv [(u - U)/U]$ at $t = 12$ h. Values are taken along the line RR' (see Fig. 1) for simulations L1 and L2, and along the line GG' otherwise. The horizontal range given on the abscissae equals the east–west extension of the innermost model domain displayed in Fig. 1. (a) Simulations with the standard orography [$\mu = 1.5$; see Eq. (1)] with $Nh_0/U = 0.3$ and various values of Na/U. The simulation W1 with $Na/U = 31$ is reproduced from Zängl (2002b). (b) Simulations with the $\mu = 1$ orography. Unlike in (a), h_0/a is kept fixed in (b).

where ρ denotes the density and $F(\mu)$ is $\pi/4$ for $\mu = 1$ (Smith 1979) and $8/(3\pi)$ for $\mu = 1.5$. The surface wind perturbation $u' \equiv [(u - U)/U]$ is normalized by the basic-state wind speed. The location where the surface wind maximum is attained is also indicated in Table 2. It is denoted as $x'_{\max}$ with x' being defined as x/L.

Except for Fig. 2 and the wide-ridge simulations reproduced from Zängl (2002b), the flow over the ridge is always considered along the line RR' (see Fig. 1), corresponding to the center of the northern mountain ridge if a gap is present. The gap flow results are taken along the line GG' (Fig. 1). The wide-ridge simulations without a gap (W1r–W4r) are also evaluated along the line GG' because the innermost model domain covers only part of the ridge in these simulations (see Zängl 2002b for details). A comparison of the no-gap simulations L1r, L2r, N1r, and N2r with the corresponding standard simulations (Table 2) indicates that the impact of the gap on the flow over the adjacent ridge(s) is very small. As will be shown below, the most notable effect is found on the upstream side of the mountain, where the presence of the gap reduces the mountain-induced blocking. Moreover, for the no-gap simulations, it makes very little difference whether line RR' or line GG' is considered (Table 2). This indicates that the mountain ridge can be considered as quasi-two-dimensional although its meridional extension is limited.

a. Linear parameter range

Before turning to the effects of strong nonlinearity, simulations for the linear parameter range are presented. The nondimensional mountain height Nh_0/U considered here ranges between 0.12 and 0.3 (see Table 1, series L and S). For this parameter setting, the flow over wider mountains is known to be qualitatively similar to linear analytical solutions. In particular, gravity wave breaking does not occur for such low mountains. Figure 2 displays the surface wind perturbation u' for a number of simulations. The values are taken along the line GG' (see Fig. 1) for all no-gap simulations (L1r, W1r, S1r–S4r) and along the line RR' otherwise. Vertical cross sections for potential temperature and the ridge-normal horizontal wind component are shown in Fig. 3. As already mentioned, Table 2 summarizes the normalized surface pressure drag and the maximum surface wind perturbation for all simulations.

First of all, the L1 and L1r wind profiles displayed in Fig. 2a indicate that the presence of a gap primarily affects the wind field on the upstream side of the mountain ridge. The maximum negative wind perturbation and the upstream extension of the area with significantly reduced wind speeds are larger in L1r than in L1. In the lee of the mountain, there are also some minor differences, but they are not as systematic as those on the upstream side. Yet, the strength of the primary wind maximum at the mountain peak hardly differs between the two runs. This is also valid for the other simulations conducted in this study (see Table 2). Since the normalized pressure drag across the ridge is also quite insensitive to the presence of a gap (Table 2), the no-gap simulations will not be discussed separately in the remainder of the paper.

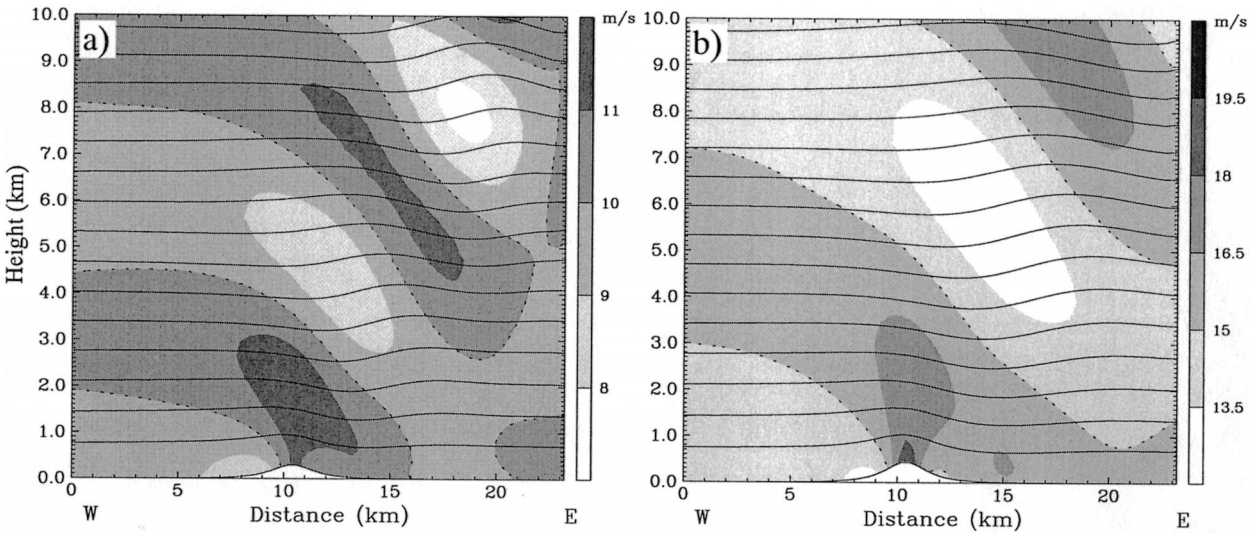

FIG. 3. Vertical cross sections of potential temperature (solid lines, contour interval 2 K) and horizontal wind speed (shading; see label bars) for the innermost model domain, $t = 12$ h. The cross sections are taken along the line RR' in Fig. 1. The dashed lines mark the prescribed large-scale wind speed U. (a) Simulation L1 ($Nh_0/U = 0.3$, $Na/U = 1.15$, $U = 10$ m s^{-1}). (b) Simulation L2 ($Nh_0/U = 0.3$, $Na/U = 0.77$, $U = 15$ m s^{-1}).

Figure 2a also gives a first impression how the mountain-induced wind perturbations depend on the mountain width. The W1r run with $Na/U \approx 31$, reproduced from Zängl (2002b) for comparison, exhibits a single wind minimum on the upstream side and a single wind maximum in the lee. When Na/U is reduced to 1.15 (run L1), the flow behavior upstream of the mountain is fairly similar, but there are now two wind maxima. The leeside wind maximum is shifted downstream, and an additional wind maximum appears at the mountain top. Moreover, the magnitude of the leeside wind maximum is only half as large as for the wide mountain, and less than that of the mountain-top wind maximum. A further reduction of Na/U to 0.77 (run L2) retains the double wind maximum structure. However, the mountaintop wind maximum becomes much stronger and the leeside maximum shifts even farther into the lee, while the wind speed reduction on the upstream side of the ridge is somewhat less pronounced. Comparing the results of L1 and L2, one finds that a reduction of Na/U by a factor of 1.5 increases the ratio between the two wind maxima by a factor of 2.5 (see also Table 2). A detailed discussion of the parameters controlling this flow behavior will be given below. Along with the intensification of the primary wind maximum at the mountain crest, the pressure drag exerted by the mountain decreases (see again Table 2). This behavior can easily be explained by linear theory since the pressure perturbation p' is proportional to $-u'$ (e.g., Smith 1979). Thus, a more symmetric wind perturbation (with respect to the crest) is equivalent to a more symmetric pressure perturbation or to a weaker pressure difference between the two sides of the mountain.

The structure of the gravity waves excited by the narrow mountain ridges is displayed in Fig. 3. Most importantly, wind and temperature perturbations are found not only above the mountain but also in the lee. This is related to the fact that nonhydrostatic gravity waves are dispersive. The slope of the group velocity vector is m/k, where m and k are the vertical and the horizontal wavenumbers, respectively, which means that the downstream component of the group velocity increases with decreasing horizontal wavelength (e.g., Smith 1979, p. 108). A consequence of this dispersion is that the leeside wind maximum is weaker for narrow mountains than for wide mountains (see Fig. 2a). Moreover, the wave amplitude would decrease with height if the dispersion effect was not compensated for by the decreasing density. In addition, it is important to note that vertical wave propagation is restricted to horizontal wavelengths longer than $2\pi U/N$ (6.28 km for $U = 10$ m s^{-1}), so that only part of the wave spectrum excited by the mountain is able to propagate vertically. As a result, the horizontal wavelength of the vertically propagating wave appears longer than the dimensions of the mountain, particularly for L2 (Fig. 3b). The wave amplitude is clearly lower for L2 (Fig. 3b) than for L1 (Fig. 3a) because a smaller part of the wave spectrum excited by the mountain propagates vertically.

It would be desirable to compare these results with linear analytic solutions, but these are available for the hydrostatic limit only in the case of $\mu = 1.5$. Thus, additional simulations (S1r–S4r) were conducted with a $\mu = 1$ mountain ridge. The normalized analytic wind perturbation obtained for this orography type in the nonhydrostatic limit is

$$u' = \frac{h_0}{a} \frac{1 - (x/a)^2}{[1 + (x/a)^2]^2} \tag{4}$$

(e.g., Smith 1979); u'_{max} is attained at the mountain peak and amounts to h_0/a. Moreover, an approximate analytical solution for $Na/U = 1$ was calculated by Queney (1948; Fig. 1). It predicts a double wind maximum similar to that discussed above. The wind extrema are $u'_{max} \approx 0.2Nh_0/U$ at the peak and $u'_{min} \approx -0.2Nh_0/U$ on the upstream side.

The results of the simulations S1r–S4r are displayed in Fig. 2b. Experiment S1r, conducted with $Na/U = 1$ for comparison with the Queney solution, shows a good qualitative agreement with the analytical result: both wind maxima and the upstream wind minimum are located at approximately the same location as in Fig. 1 of Queney (1948). The gravity wave pattern, which is very similar to that shown in Fig. 3a, is also consistent with the analytical solution. However, the magnitude of the simulated surface wind perturbations is substantially larger. While the analytical solution predicts $u'_{min} \approx -0.06$ and $u'_{max} \approx 0.06$ for the mountain height under consideration, the numerical simulation yields values of -0.17 and 0.15, respectively. Nonlinear effects are unlikely to be responsible for this large discrepancy: additional experiments with mountain heights of 100, 10, and 1 m consistently exhibited wind perturbations 2–2.5 times as large as predicted by the analytical solution. Moreover, the simulations for wider and narrower mountain ridges do not indicate the presence of a systematic model error. The difference between the wind perturbations predicted by the hydrostatic analytical solution (Phillips 1984) and the simulations reported in Zängl (2002b) is only about 30% for $Nh_0/U = 0.3$ and tends to approach zero for very low mountains. In addition, the simulations with $Na/U < 1$, which will be discussed below, approach the analytical solution for the nonhydrostatic limit [Eq. (4)]. A possible explanation for the large discrepancy between the Queney (1948) result and the simulations could be that the asymptotic solution technique applied by Queney is not particularly exact close to the ground.

Simulations S2r and S3r investigate the effect of reducing Na/U to 0.67 and 0.4 while keeping h_0/a constant at 0.3. This is associated with a decrease of the nondimensional mountain height Nh_0/U from 0.3 to 0.2 and 0.12, respectively. As evident from Fig. 2b, the wind reduction on the upstream side of the ridge weakens, the mountaintop wind maximum intensifies and the leeside wind maximum weakens and shifts farther downstream. The intensification of the mountaintop wind maximum despite the decreasing Nh_0/U clearly demonstrates that this wind maximum does not scale with Nh_0/U, which is in agreement with Eq. (4) for the nonhydrostatic limit. Moreover, the simulated values for u'_{max} (Table 2) indicate that the simulations would approach the analytical value of $h_0/a = 0.3$ for even smaller Na/U. A check whether u'_{max} does really scale with h_0/a as predicted by Eq. (4) is provided by a comparison between S2r and S4r. Increasing h_0/a by 50% while keeping Na/U fixed increases u'_{max} by about 60% (see also Table 2), suggesting that there are probably some nonlinear effects but that the scaling law for the nonhydrostatic limit is already valid in the transitional parameter range of $Na/U \approx 1$. Yet, the leeside wind maximum is still, to a large extent, controlled by Nh_0/U. Simulations S1r and S4r, differing in Na/U but having the same Nh_0/U, show only a slight weakening of the leeside maximum with decreasing Na/U. This is confirmed by the simulations L1 and L2 already discussed above. On the other hand, the series S1r–S3r (fixed h_0/a) exhibits a much stronger weakening of the leeside wind maximum. The apparent explanation for this behavior is that the leeside wind maximum is related to the vertically propagating part of the wave spectrum, which is known to scale with Nh_0/U from hydrostatic analytical solutions. This is corroborated by the fact that the leeside wind maximum shifts downstream with decreasing Na/U. Since vertical propagation requires a horizontal wavelength larger than $2\pi U/N$, the nondimensional location of the leeside wind maximum x'_{max} can be expected to be inversely proportional to Na/U if $Na/U \lesssim 1$. Finally, considering the wind speed upstream of the mountain reveals that the upstream effect depends on both Na/U and on Nh_0/U. Because the analytical values of u'_{min} are $h_0/(8a)$ for the nonhydrostatic limit and $Nh_0/(2U)$ for the hydrostatic limit, the decrease of $|u'_{min}|$ with Na/U can easily be anticipated from analytical theory.

The drag values provided in Table 2 show that the drag decreases continuously with Na/U. This is also in agreement with linear theory since the analytical solution for the nonhydrostatic limit predicts zero drag. Comparison between S2r and S4r again indicates that nonlinear effects are small in the parameter range considered here. Moreover, a comparison between the drag und u'_{max} values for the L and S runs shows that the mountain shape has only a minor impact on the results when similar values of Na/U are considered. However, using the length scale L instead of the half-width a as control parameter would pretend a substantial influence of the mountain shape. For this reason, only a was used in the preceding discussion.

The results for the linear flow regime suggest that the gravity wave response of a narrow mountain ridge can to some extent be interpreted as a superposition of a vertically propagating wave and an evanescent wave. While the former induces a wind maximum in the lee of the mountain, the latter is responsible for the mountaintop wind maximum. The relative importance of the wave components is controlled by Na/U and changes quite rapidly with this parameter.

b. Nonlinear parameter range

For quasi-hydrostatic flow over a two-dimensional mountain ridge, gravity wave breaking sets in as soon as the nondimensional mountain height exceeds a value of about 0.85 (e.g., Peltier and Clark 1979). This leads

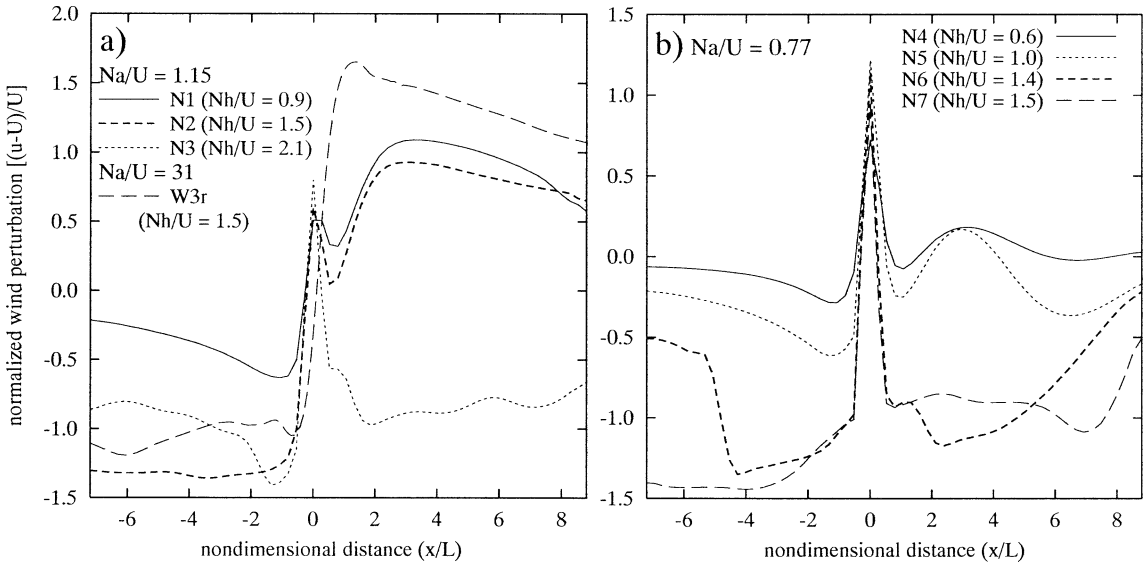

FIG. 4. Same as Fig. 2, but for simulations with higher mountains. The values are taken along the line RR' in Fig. 1 except for simulation W3r, for which the values refer to the symmetry axis of the mountain ridge.

to the formation of strong downslope winds over the lee slope of a mountain and to a pressure drag several times larger than the linear value. In this section, it is investigated whether wave breaking and the concomitant strong downslope winds also occur for $Na/U \sim 1$. Surface wind profiles similar to Fig. 2 are given in Fig. 4. In addition, vertical cross sections of the wind and potential temperature fields are displayed in Fig. 5 for four selected simulations.

For $Nh_0/U = 0.9$ and $Na/U = 1.15$ (run N1, Figs. 4a and 5a), the flow structure is indeed remarkably close to that typical for the quasi-hydrostatic flow regime (e.g., Stein 1992; Zängl 2002b). Gravity wave breaking occurs above the lee slope and forms an almost calm zone extending downstream at a height of about 2 km. Supported by the decrease of atmospheric density with height, a second wave breaking region forms at about 8 km. Correspondingly, strong downslope winds are found near the ground. In contrast to the quasi-linear simulation L1, the leeside wind maximum is now much stronger than the mountaintop wind maximum, which is noticeable in Fig. 4a only. Although the corresponding wide-ridge simulation W2r exhibits an even larger wind amplification (see Table 2 and Zängl 2002b), this clearly indicates that nonlinearity can reduce the impact of nonhydrostatic effects. The dominance of the leeside wind maximum is extended to lower values of Na/U.

Interestingly, the pressure drag depends much more sensitively on the mountain width than the leeside wind maximum. As evident from Table 2 (runs N1 and W2r), nonhydrostatic effects reduce the normalized drag by a factor of almost two, while u'_{max} decreases by only 20%. A closer investigation of the pressure field reveals that this is largely due to the fact that the leeside pressure minimum is located farther downstream for the narrow mountain than for the wide one (close to x'_{max}; see Table 2). The maximum cross-mountain pressure difference decreases only from 3.6 to 2.9 hPa (not shown), but between the peak and $x = \pm 1.5a$, the cross-mountain pressure difference decreases by a factor of more than 2.

For higher mountains (runs N2 and N3, Figs. 4a, 5b, and 5c), the impact of nonhydrostatic effects increases again. There are still strong downslope winds extending far into the lee for $Nh_0/U = 1.5$ (run N2), but the local wind maximum at $x = 0$ is more pronounced than for $Nh_0/U = 0.9$, and u'_{max} is substantially lower than for the corresponding quasi-hydrostatic run W3r (Fig. 4a and Table 2). The normalized drags again differ by a factor of two (Table 2). For $Nh_0/U = 2.1$ (run N3), the flow separates from the ground over the lee slope, and there remains only one wind maximum at the crest (Fig. 5c). The corresponding wide-mountain run W4r, however, retains its wind maximum in the lee, and flow separation is not encountered (Table 2 and Zängl 2002b). Correspondingly, the difference in the normalized pressure drag further increases.

A remarkable feature appearing in both N2 and N3 is an atypically weak gravity wave activity over the mountain. A closer examination of the flow evolution reveals that there occurs transient wave breaking during the first 2 h of the simulation, but then, the wave breaks down and the remaining upward flux of wave energy is very weak. For wider mountains, such a breakdown of the wave energy flux is usually not found (e.g., Peltier and Clark 1979; Olafsson and Bougeault 1997; Zängl 2002b). In fact, the gravity wave patterns found for the wide-mountain simulations W2r, W3r, and W4r are very similar to each other, and it is merely the depth of the leeside strong wind zone that decreases with increasing

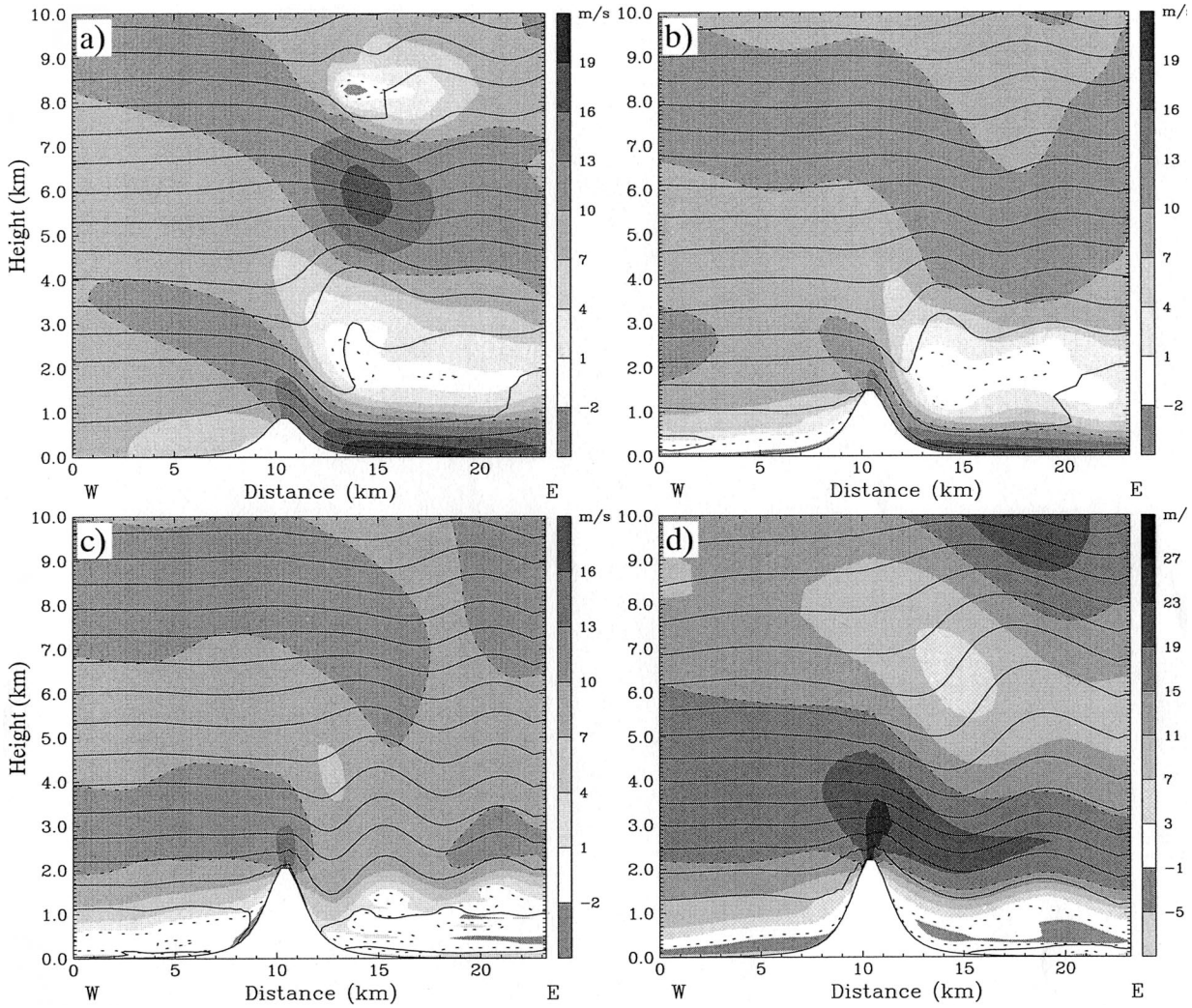

FIG. 5. Vertical cross sections along line RR' (Fig. 1) for simulations (a) N1 ($Nh_0/U = 0.9$, $Na/U = 1.15$), (b) N2 ($Nh_0/U = 1.5$, $Na/U = 1.15$), (c) N3 ($Nh_0/U = 2.1$, $Na/U = 1.15$), and (d) N7 ($Nh_0/U = 1.5$, $Na/U = 0.77$). Plotting conventions are as in Fig. 3, but dashed lines are given for $u = U$ and $u = 0$. The basic-state wind speed U is 10 m s^{-1} in (a)–(c) and 15 m s^{-1} in (d).

Nh_0/U (see Zängl 2002b). A conclusive explanation of the weak wave activity in the narrow-ridge runs is difficult to give because analytical methods are not applicable to such highly nonlinear flows. From the simulated flow evolution, it appears that the well-mixed layer established in the lee of the mountain for $Nh_0/U = 1.5$ reflects much of the wave energy while flow separation prevents the maintenance of a larger wave amplitude for $Nh_0/U = 2.1$. For the wide ridges, no flow separation occurs in this range of mountain heights, and the vertical orientation of the group velocity vector probably reduces the impact of the well-mixed region in the lee on the wave propagation.

A decrease of Na/U to 0.77 leads to a drastic change of the flow pattern as is the case for the lower mountains discussed above. None of the simulations exhibits gravity wave breaking, and the maximum wind speed is reached at the mountain crest in all simulations. Since airflow over a mountain with $Na/U \approx 1$ is controlled partly by h_0/a and partly by Nh_0/U (see discussion of Fig. 2b above), experiments N4–N7 are conducted either with the same h_0/a as runs N1–N3 or with the same Nh_0/U (see Table 1). Yet, the following discussion always refers to Nh_0/U since this is a more common nondimensional parameter than h_0/a.

As already mentioned, the wind maximum now occurs at the mountain crest for all mountain heights considered (Fig. 4b). In contrast to above, and consistent with the absence of gravity wave breaking, only a weak nonlinear wind amplification is found. Comparing the results for $Nh_0/U = 0.3$ (L2), $Nh_0/U = 0.6$ (N4), and $Nh_0/U = 1.0$ (N5) reveals that the ratio of $u'_{\max}$ and h_0 increases by no more than 20% (Figs. 2a and 4b, and Table 2). A somewhat larger increase is found for the normalized drag (Table 2), but the values remain well below 1 in all cases. When Nh_0/U is increased above

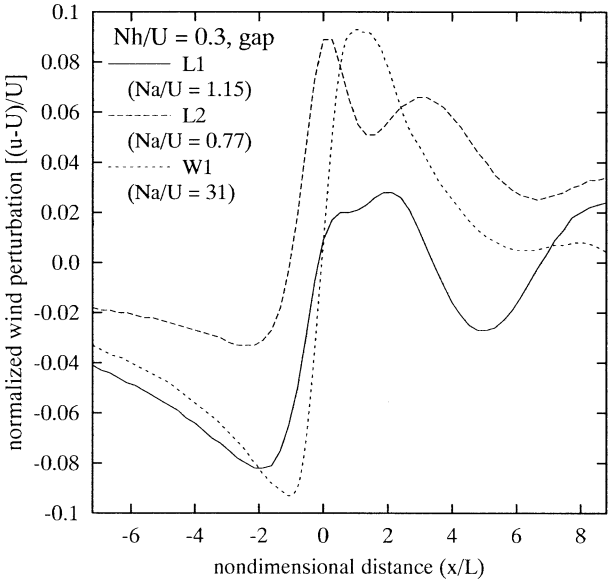

FIG. 6. Same as Fig. 2a, but values along the gap axis (line GG' in Fig. 1).

1.0, u'_{max} and the normalized drag decrease again (runs N6, $Nh_0/U = 1.4$, and N7, $Nh_0/U = 1.5$). This can be explained by upstream blocking, which reduces the effective mountain height. A similar behavior has often been reported for quasi-hydrostatic flow over wide mountains (e.g., Olafsson and Bougeault 1996; Bauer et al. 2000). It is interesting to note that the vertically propagating gravity wave visible in Fig. 5d has a substantially larger amplitude than the waves found in simulations N2 and N3 with $Na/U = 1.15$ (Figs. 5b,c). As already mentioned above, initial wave breaking is followed by an almost complete breakdown of the upward wave energy flux in simulations N2 and N3. At later times, the wave activity remains weak regardless whether a strong downslope flow is maintained (Fig. 5b) or not (Fig. 5c). For $Na/U = 0.77$, the permanent absence of wave breaking appears to preclude a breakdown of the wave energy flux. Another interesting feature is that the dependence of the normalized drag on Na/U becomes weak when the mountain is high enough for flow separation to occur over the lee slope. The simulations N3, N6, and N7, which all have virtually no surface wind in the lee of the mountain (Fig. 4), also exhibit very similar drag values (Table 2).

c. Gap effects

Since real mountain ridges are usually not quasi-two-dimensional, it is certainly justified to investigate the effects of gaps in narrow mountain ridges. The discussion again starts with the linear flow regime and then considers the ridge heights that were found to induce wave breaking in the previous section. Surface wind profiles along the line GG' in Fig. 1 are displayed in Fig. 6 for the linear flow regime and in Fig. 8 for the nonlinear flow regime. Vertical cross sections of wind and potential temperature are given in Figs. 7 and 9, respectively. Finally, Fig. 10 shows the horizontal wind field at 250 m AGL for two cases.

As evident from Fig. 6, the wind perturbations along the gap axis are qualitatively similar to those found over the mountain ridges (Fig. 2a) in that there is a negative wind perturbation on the windward side and a positive wind perturbation in the lee. However, their magnitude is substantially weaker than for the ridge, and the spatial structure of the wind perturbations partly differs from those above the ridge. Most importantly, a local wind maximum at $x' = 0$ (i.e., in the gap center) is missing in L1 ($Nh_0/U = 0.3$, $Na/U = 1.15$), so that there is just

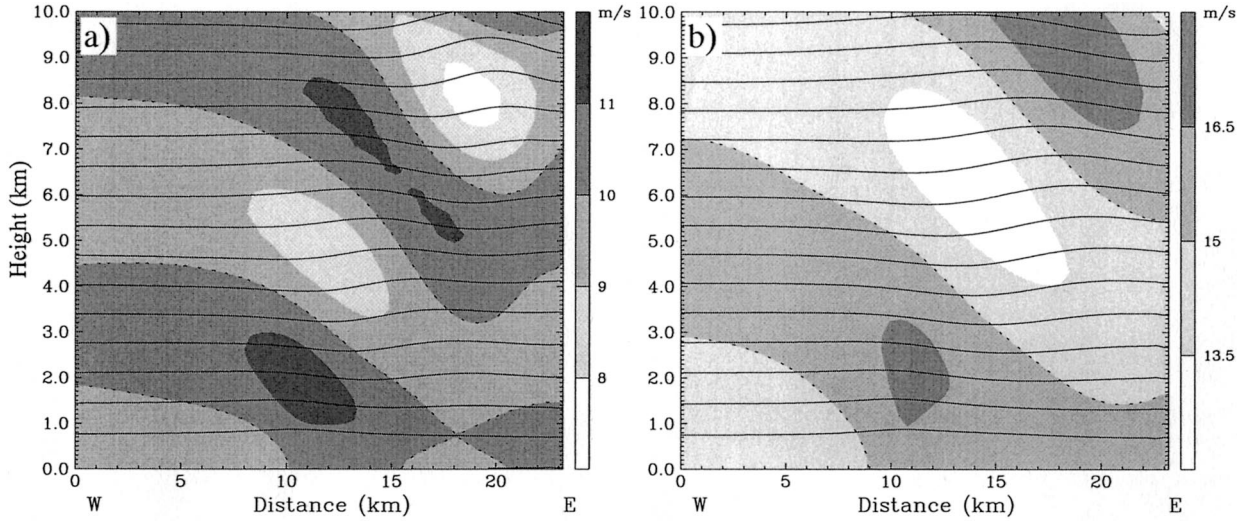

FIG. 7. Same as Fig. 3, but for cross section GG' along the gap axis. The simulations are (a) L1 ($Nh_0/U = 0.3$, $Na/U = 1.15$) and (b) ($Nh_0/U = 0.3$, $Na/U = 0.77$).

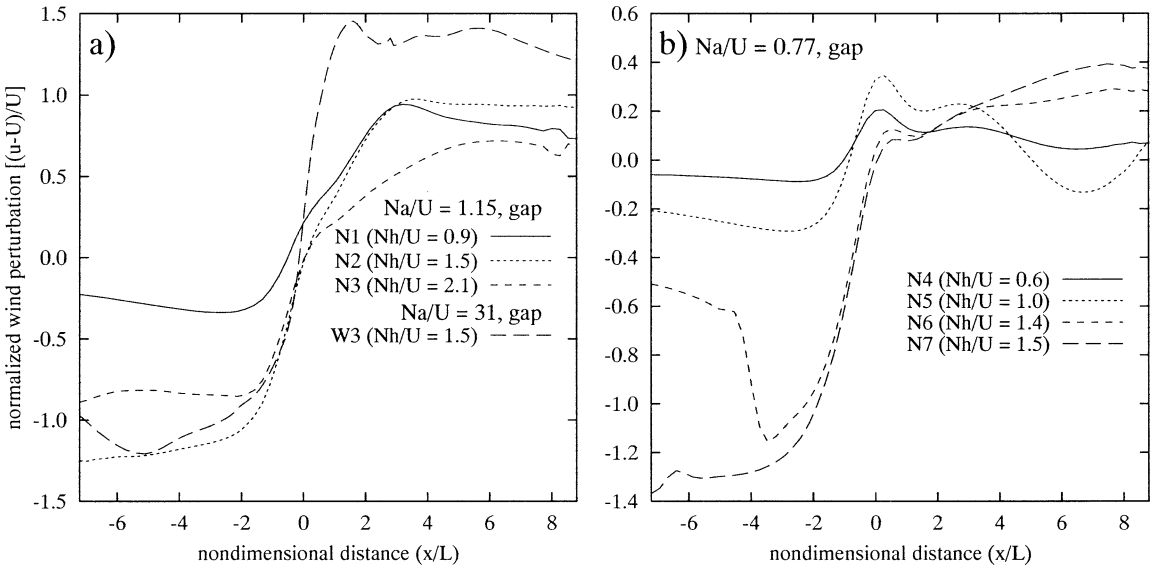

FIG. 8. Same as Fig. 4, but values along the gap axis (line GG' in Fig. 1).

a single wind maximum in the lee. The maximum wind perturbation u'_{max} is less than 25% of that found for the ridge (see Table 2), but u'_{min} is roughly half as large as for the ridge. Simulation L2 ($Nh_0/U = 0.3$, $Na/U = 0.77$) exhibits two wind maxima along the gap axis, the primary one being at $x' = 0$, as is the case for the ridge. However, the dominance of the wind maximum at $x' = 0$ is less pronounced for the gap than for the ridge. The closest structural agreement between the wind perturbations along the gap axis and those above the ridge is found for the wide-ridge simulation W1r. The gap–ridge ratios of u'_{max} (u'_{min}) are 43% (52%) in this case.

The qualitative similarity between the wind perturbations along the gap axis and those above the mountain ridge can be explained by the intrinsically three-dimensional structure of the flow. As already discussed in Zängl (2002b), low-level confluence in the gap region causes the negative wind perturbation generated on the windward side of the mountain ridges to extend into the gap region. Moreover, the properties of gravity wave propagation over three-dimensional topography make an important contribution. Vertically propagating gravity waves excited by a localized mountain are subject to a horizontal dispersion in cross stream direction, regardless whether the flow is hydrostatic or nonhydrostatic (Smith 1980; Zängl 2002b). Thus, the gravity waves excited by the mountain ridges spread out toward the gap, and at some vertical distance from the ground, the wave pattern above the gap axis becomes very similar to that above the adjacent mountain ridges (Fig. 7, cf. Fig. 3). Correspondingly, the wind perturbations related to the gravity waves can also be found above the gap axis (Fig. 7).

It remains to be discussed why the relative magnitude of the wind perturbations along the gap axis is lower for narrow ridges than for wider ones. First, a comparison of Figs. 3 and 7 suggests that the wave dispersion is more effective for the vertically propagating part of the wave spectrum than for the decaying one. Although the lack of exact analytical solutions precludes a proof of this hypothesis, it is at least plausible that a rapidly decaying disturbance has less chance to spread out into the gap than a propagating one. As a consequence, one expects that the tendency for a wind maximum at $x' = 0$ is less pronounced along the gap axis than above the adjacent ridge. This is in agreement with the numerical results. Second, the wave dispersion in along-flow direction related to nonhydrostatic effects might play a role. It tends to weaken the wave signal that reaches the gap axis and thus contributes to the reduced gap–ridge ratios of the leeside wind maxima. On the other hand, the low-level confluence on the upstream side of the gap is not directly related to the properties of wave propagation. This might explain why u'_{min} is quite similar for L1 and W1r. However, the large difference between L1 and L2 indicates that there are further processes not yet recognized.

When the adjacent mountain ridge is high enough to induce wave breaking, the flow structure along the gap axis undergoes major changes. Part of these changes is similar to those found above the ridge, but there are also some pronounced differences. For $Na/U = 1.15$ (Fig. 8a), all experiments show a strong wind amplification in the lee of the gap. In cases N1 ($Nh_0/U = 0.9$) and N2 ($Nh_0/U = 1.5$), this is in agreement with what was found for the adjacent ridges (see Fig. 4a), but in simulation N3 ($Nh_0/U = 2.1$), the strong wind is restricted to the gap area and thus appears as a localized jet (see also Fig. 10a). This indicates that the tendency toward a strong wind maximum in the lee is even more pronounced for a gap than for a quasi-two-dimensional ridge. Moreover, none of the cases exhibits a local gap

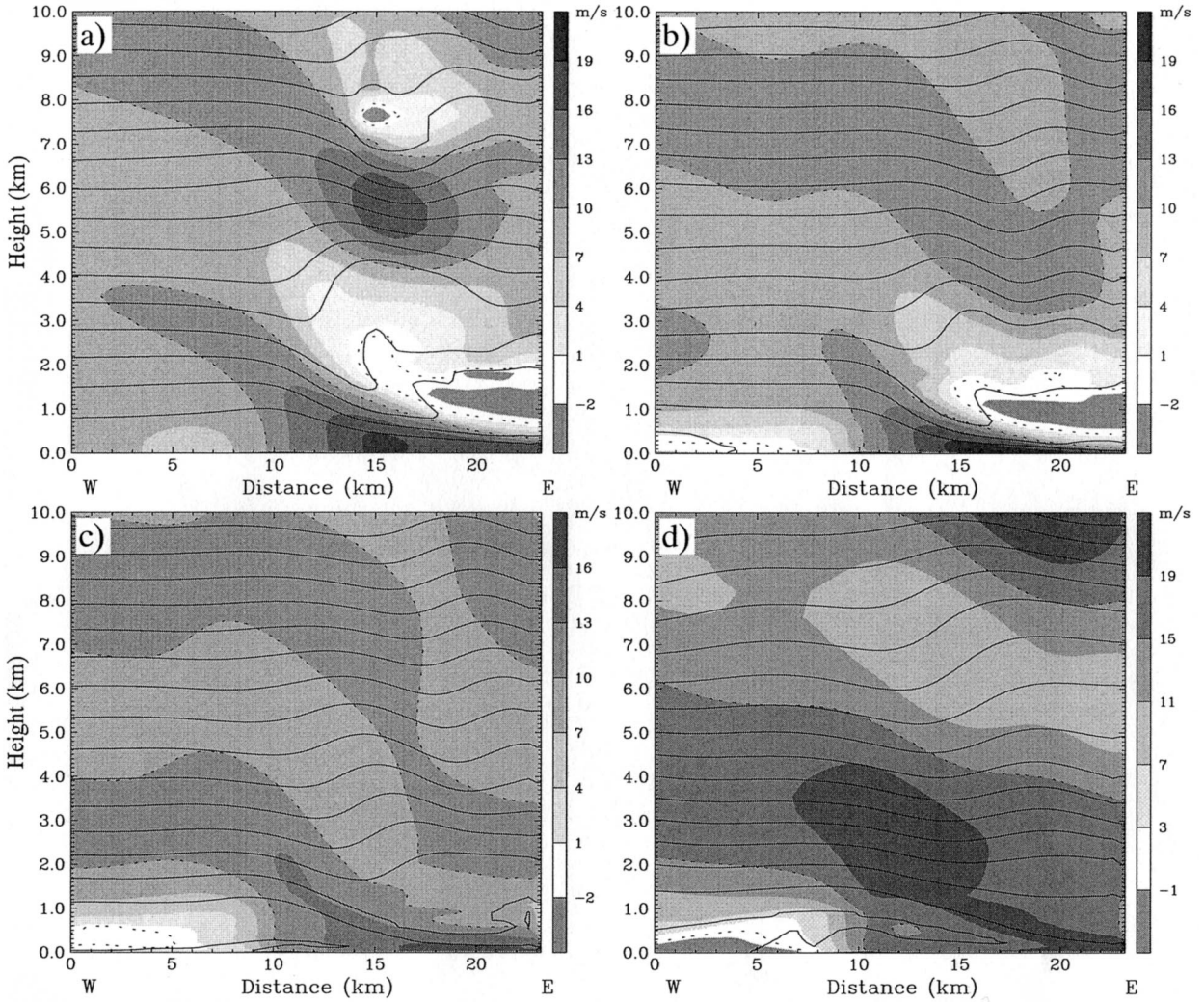

FIG. 9. Same as Fig. 5, but for cross section GG' along the gap axis. The simulations are (a) N1 ($Nh_0/U = 0.9$, $Na/U = 1.15$), (b) N2 ($Nh_0/U = 1.5$, $Na/U = 1.15$), (c) N3 ($Nh_0/U = 2.1$, $Na/U = 1.15$), and (d) N7 ($Nh_0/U = 1.5$, $Na/U = 0.77$).

wind maximum at $x' = 0$, so that the flow structure along the gap axis is qualitatively similar to the wide-ridge experiment W3 ($Nh_0/U = 1.5$, Fig. 8a). This is, again, in contrast to the results found for the mountain ridge (Fig. 4), showing a pronounced wind maximum at $x' = 0$ at least for N2 and N3. A comparison between experiments W3 and N2 (both $Nh_0/U = 1.5$) shows that u'_{max} is still lower for N2 than for W3, but the relative difference is much smaller than for the low-mountain simulations L1 and W1. It can be concluded that nonlinear effects greatly reduce the dependence of gap flows on the width of the adjacent mountain ridges. Moreover, the range of nondimensional mountain heights for which nonhydrostatic effects lose their impact on the flow structure is larger along a gap axis than for a mountain ridge.

The vertical cross sections along the gap axis (Figs. 9a–c) show that the gravity wave fields above the gap axis are very similar to those above the mountain ridge (Figs. 5a–c) except for the lowermost 2 km. This can again be explained by the cross-stream wave dispersion discussed above. However, the weakness of the gravity wave activity for $Nh_0/U \geq 1.5$ raises the question of which dynamical mechanism accelerates the flow through the gap. In agreement with the findings made by Zängl (2002b), a detailed analysis of the model results suggests that the pressure field driving the gap flow is no longer directly related to the gravity wave pattern aloft. Rather, the larger-scale cross-mountain pressure difference built up by blocking effects and the flow field over the adjacent ridges becomes relevant as soon as the flow gets strongly nonlinear. As demonstrated in Figs. 6 and 10 of Zängl (2002b), the cross-mountain pressure difference then extends into the gap region without significant weakening, regardless of the local gravity wave field above the gap axis. In the simulations

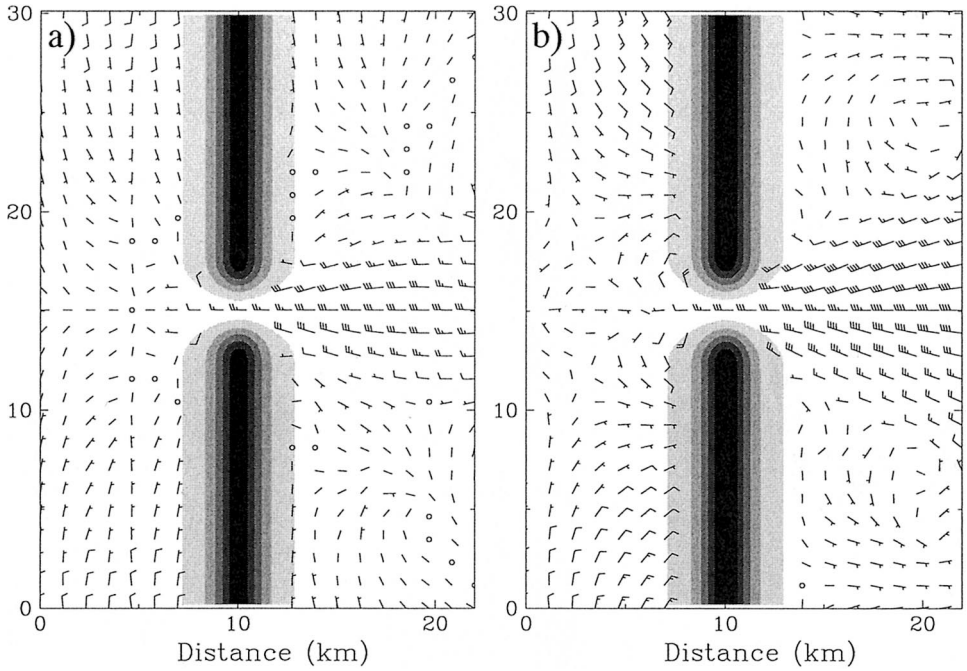

FIG. 10. Horizontal cross section at a constant height of 250 m for simulations (a) N3 ($Nh_0/U = 2.1$, $Na/U = 1.15$) and (b) N7 ($Nh_0/U = 1.5$, $Na/U = 0.77$). A full barb denotes a wind speed of 5 m s^{-1}. Orography shading starts at 200 m with shading steps every 400 m.

considered here, the maximum pressure difference along the gap axis is 2.2, 2.4, and 1.75 hPa for nondimensional mountain heights of 0.9, 1.5, and 2.1, respectively. For these pressure differences Δp and a density of $\rho = 1.2$ kg m^{-3}, the Bernoulli equation for a surface streamline

$$\frac{u^2}{2} - \frac{u_o^2}{2} = \frac{\Delta p}{\rho} \tag{5}$$

predicts maximum wind speeds of 20.2, 20.0, and 17.1 m s^{-1}, respectively, when u_o is taken to be 6.5 m s^{-1} for $Nh_0/U = 0.9$ (see Fig. 8a), and 0 m s^{-1} otherwise. This is in close agreement with the simulated values of $u_{\max}$ (19.4, 19.7, and 17.2 m s^{-1}, in dimensional form) when taking into account that some of the momentum may be lost in N1 and N2 due to vertical mixing with the weak wind layer aloft. The dominant influence of the cross-mountain pressure difference provides a good explanation why nonlinear gap flow dynamics is so insensitive to the mountain width and the related properties of the gravity waves.

Apart from this, the cross sections for the runs N1 and N2 (Figs. 9a,b) suggest that hydraulic dynamics—that is, conversion of potential energy into kinetic energy—could play a role in establishing the leeside wind maximum (cf. Arakawa 1969). Although the large-scale flow prescribed in the simulations is uniform, interactions with the orography form an almost neutral surface layer capped by a stable layer, so that the reduced gravity shallow water theory (Drobinski et al. 2001 and references therein) may be applied to this flow problem. Unfortunately, the lack of an inversion makes it hardly possible to compute a Froude number on the upstream side of the gap, but the flow on the lee side is clearly supercritical. Assuming an inversion strength $\Delta\theta$ of 4 K, a mean potential temperature $\overline{\theta}$ of 290 K and a flow depth H of 750 m, the Froude number

$$\frac{U}{\sqrt{g(\Delta\theta/\overline{\theta})H}} \tag{6}$$

(see Drobinski et al. 2001) exceeds 1 for $U > 10$ m s^{-1}, which is easily fulfilled in the lee of the gap. A hydraulic-jump-like feature is found outside the model domain shown in Fig. 9. It is mentioned that the interpretation of gap flows in terms of hydraulic theory often helps to better understand the complex behavior of nonlinear gravity wave dynamics. As recently shown by Flamant et al. (2002), the local structures of gap flows in a valley with varying width can be well reproduced and interpreted with a simple hydraulic model, supporting the analysis of full-physics numerical models.

Turning to the results for $Na/U = 0.77$ (runs N4–N7; Figs. 8b, 9d, and 10b), it is important to note that the flow can be considered as quasi linear up to $Nh_0/U = 1.0$ (run N5) for such a narrow mountain. As discussed in section 3b, the wind perturbations induced by the mountain ridge increase roughly linearly with h_0 in this parameter range. Evidently, this is also valid for the maximum wind perturbation along the gap axis (Fig. 8b and Table 2), which is attained at $x' = 0$ as in the L2 run (Fig. 6). For higher mountains (runs N6, $Nh_0/U =$

1.4 and N7, $Nh_0/U = 1.5$), the absence of wave breaking still precludes the build up of a strong cross-mountain pressure difference, so that the maximum wind speed along the gap axis remains comparatively weak (cf. Figs. 8b and 8a). Yet u'_{max} is now reached far downstream of the gap center (see also Table 2), and the wind maximum at $x' = 0$ disappears. Thus, the flow structure becomes, again, qualitatively similar to that typical for gaps embedded in wide mountain ridges. Moreover, the formation of an almost calm wake in the lee of the ridge makes the gap flow appear as a localized jet (Fig. 10b). It is mentioned that the acceleration of the flow through the gap in N6 and N7 is again consistent with the cross-mountain pressure difference built up by the partially blocked flow over the adjacent ridges.

It is interesting to check whether the wake formation in the lee of the mountain ridge found for N3, N6, and N7 is associated with lee vortices. An analysis of the flow in the coarser model domains reveals that none of the simulations exhibit lee vortices on the scale of the whole mountain ridge (not shown). The shear lines separating the wake from the flow around the ridge run almost straight and meet each other in the far lee of the mountain ridge. Since wake formation in the lee of wide mountain ridges is usually associated with rather pronounced lee vortices (e.g., Olafsson and Bougeault 1997; Zängl 2002b), this suggests that the tendency of shear lines to roll up to a vortex decreases with their horizontal scale. There are, however, cases exhibiting small-scale vortices in the lee of the gap. The horizontal cross section at $z = 250$ m displayed in Fig. 10b (run N7) shows a pair of vortices in the lee of the gap, and a similar result is found for N6 (not shown). On the other hand, no local lee vortices occur in run N3 (Fig. 10a). We have to conclude that there are certainly more factors influencing the formation of lee vortices than just the scale of the shear line, but an exhaustive investigation of lee vortex dynamics is beyond the scope of this paper.

d. Experiments with surface friction

Apart from a general reduction of the near-surface wind speed, surface friction is known to lower the gravity wave amplitudes and to reduce the tendency toward wave breaking (e.g., Georgelin et al. 1994; Olafsson and Bougeault 1997). Moreover, friction tends to force flow separation from the ground over the lee slope of a mountain, particularly when wave breaking occurs despite friction and the flow is in a high-drag state (e.g., Richard et al. 1989, 1990). The tendency for flow separation has been found to be less pronounced along gaps than in the lee of a mountain ridge (Zängl 2002b). In addition, Doyle and Durran (2002) showed that the friction-induced flow separation is essential for the formation of rotors. In this section, the impact of surface friction on airflow over a narrow mountain ridge is investigated. It will turn out that part of the frictional effects is similar to that known for wider ridges. However, there is a significant range of mountain heights for which friction leads to a larger amplitude of the vertically propagating gravity waves. An interesting and novel discovery is that the formation of leeside rotors is possible even for uniform upstream flow.

As mentioned in section 2, roughness length values of 1 and 50 cm have been prescribed in the frictional simulations, corresponding to grassland and forest, respectively. While a value of 50 cm turned out to prevent the occurrence of wave breaking for all mountain heights considered in this study, wave breaking is still possible for a roughness length of 1 cm. For low mountains, the impact of the surface friction is largely restricted to a reduction of the wind speed close to the ground. Thus, the following discussion starts with a nondimensional mountain height of 0.9. Selected surface wind profiles for the mountain ridge and the gap axis are given in Fig. 11. Unlike above, dimensional wind speeds are shown in this figure because friction renders the unperturbed surface wind speed different from U and thus makes the normalized wind perturbation u' difficult to interpret. Since all simulations discussed in the following are based on $U = 10$ m s^{-1}, a normalization of the wind speed is not needed for comparability. Figure 12 depicts vertical cross sections of wind and potential temperature for the simulations with $Nh_0/U = 1.5$. A closer look at the rotor found in the N21f simulation is provided in Fig. 13.

As evident from Fig. 11a, all simulations with a roughness length of 50 cm attain their primary wind maximum at the mountain crest. For $Nh_0/U = 0.9$ (run N1f), a significant secondary wind maximum occurs in the lee, but for the higher mountains, flow separation is forced immediately behind the mountain crest. In the latter cases, very weak winds are found in the lee of the mountain ridge. The tendency toward flow separation also has the consequence that the pressure drag is 30%–40% lower than in the frictionless runs except for N3 ($Nh_0/U = 2.1$), where flow separation even occurs without friction (not shown). Along the gap axis, however, the wind maxima generally occur in the lee as in the quasi-hydrostatic case (Fig. 11b). For $Nh_0/U = 0.9$, the maximum gap wind speed is somewhat weaker than the secondary wind maximum in the lee of the ridge, but otherwise, the gap flow appears as a localized jet. It is interesting to note that the maximum gap wind speed does not increase between $Nh_0/U = 0.9$ (N1f) and $Nh_0/U = 1.5$ (N2f) while it increases by about 50% between $Nh_0/U = 1.5$ and $Nh_0/U = 2.1$ (N3f). A closer analysis of the simulations suggests that hydraulic dynamics (conversion of potential into kinetic energy) supports the formation of the pronounced wind maximum for $Nh_0/U = 2.1$ (not shown). For $Nh_0/U = 1.5$, however, such an effect is missing (Fig. 12b). The N2f simulation also allows for a comparison with an otherwise identical simulation with $Na/U = 31$ (Zängl 2002b, Fig. 10). The maximum wind speed above the mountain

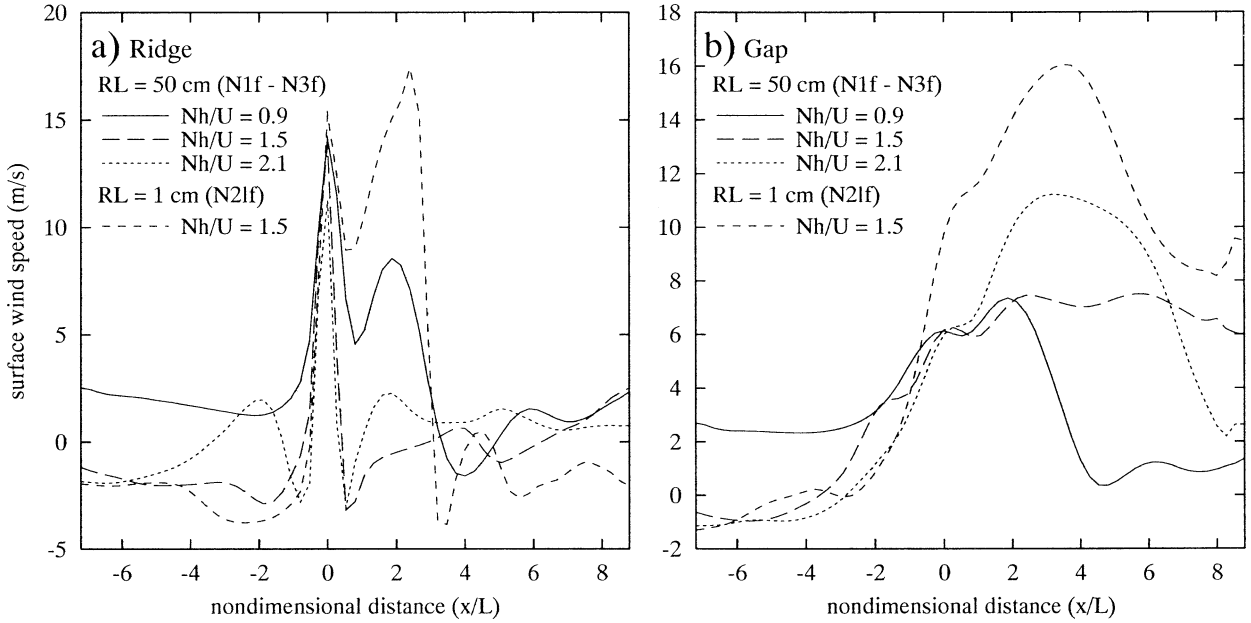

FIG. 11. Same as Figs. 4a and 8a, but for simulations with surface friction. The wind profiles are taken (a) along line RR' and (b) along line GG' (see Fig. 1 for location). Roughness lengths and nondimensional mountain heights are indicated in the figures.

ridge (14 m s^{-1}) is almost identical to that obtained for the wide mountain. However, it occurs at the mountain crest for the narrow mountain but in the lee for the wide one. The maximum gap wind speed is 7.5 m s^{-1} compared to 9 m s^{-1}. Another interesting feature of the N2f simulation is revealed by Fig. 12a. Compared with the corresponding frictionless run (Fig. 5b), the amplitude of the vertically propagating gravity waves is substantially larger. While the wave energy flux breaks down after about 2 h of simulation in the frictionless run (see discussion in section 3b), the simulation with friction remains in the quasi-linear regime without wave breaking and a rather large vertical flux of wave energy. This behavior has also been found for $Nh_0/U = 2.1$ (not shown). To the author's knowledge, none of the existing studies on the effects of surface friction indicate that friction can also lead to an *increase* of the quasi-stationary gravity wave amplitude. This is related to the fact that wave breaking usually does not lead to a breakdown of the wave energy flux.

When the roughness length is reduced to 1 cm, the primary wind maximum shifts from the mountain crest to the lee except for $Nh_0/U = 2.1$, where flow separation occurs even in the frictionless case (shown for $Nh_0/U = 1.5$ only). For $Nh_0/U = 1.5$ (run N2lf), the maximum wind speed along the gap axis more than doubles and is close to the maximum speed in the lee of the ridge (Fig. 11). Figure 12d indicates that a hydraulic-like conversion of potential into kinetic energy contributes to this strong wind maximum. The Froude number computed according to Eq. (6) is well above 1 in the lee of the gap, and a weak indication of a hydraulic jump is also visible. Yet, the pronounced gravity wave activity above the gap axis makes the impact of hydraulic dynamics less evident than in the frictionless cases discussed above. Most interestingly, the cross section through the mountain ridge (Fig. 12c) shows the formation of rotors in the lee of the ridge (see also Fig. 13 for a zoomed view), a phenomenon that has recently regained great scientific interest (see Doyle and Durran 2002 and references therein). While the first (counterclockwise) rotor is related to gravity wave breaking, the second (clockwise) one closely resembles the "classical" rotors occurring beneath wave crests of trapped lee waves (Doyle and Durran 2002). The turbulent kinetic energy field displayed in Fig. 13 indicates substantial turbulence in both rotors, making them potentially hazardous to aviation in the same way as the classical rotors. In contrast to what has been known so far, the rotors form despite the fact that the large-scale flow is uniform and thus does not support linear trapped lee waves. It appears that nonlinear interactions between the various parts of the nonhydrostatic gravity wave spectrum set up an environment supporting the formation of the second rotor. As confirmed by Fig. 12a, the wind perturbations induced by the upward propagating part of the wave spectrum are capable of partly trapping the more horizontally propagating modes because they induce a local decrease of the Scorer parameter N/U. Moreover, the hydraulic jump occurring at the foot of the mountain ridge might play an important role since it produces a dipole of horizontal vorticity. This vorticity rolls up to form a pair of rotors. The hypothesis that nonlinear effects are crucial for the development of the rotors is supported by experiments with lower mountains (not shown). Run N1lf ($Nh_0/U = 0.9$) also exhibits wave

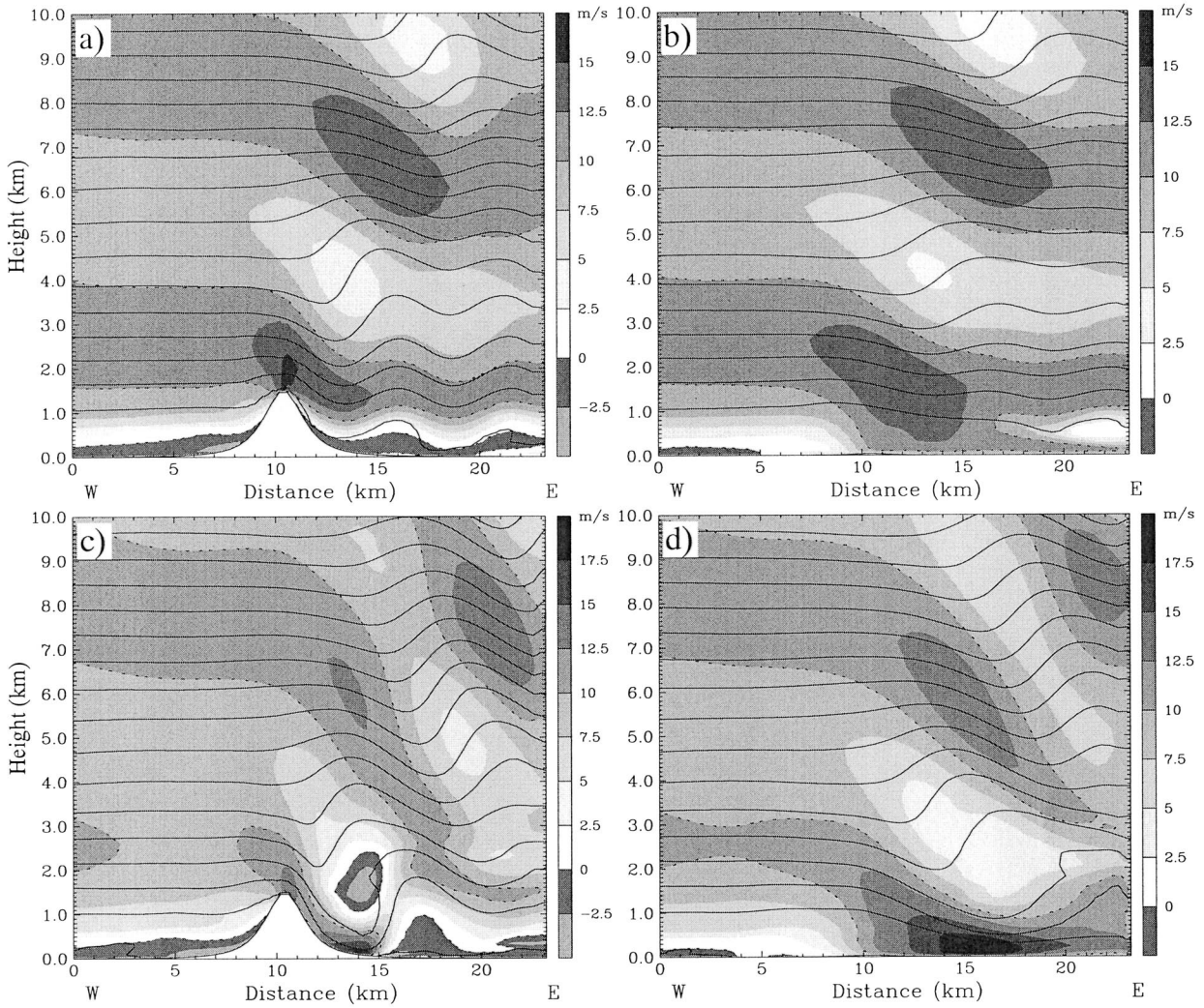

FIG. 12. Same as Fig. 5, but for simulations with surface friction and $Nh_0/U = 1.5$. (upper row) simulation N2f (roughness length = 50 cm), cross sections along line (a) RR' and (b) GG'; (lower row) simulation N2lf (roughness length = 1 cm), cross sections along line (c) RR' and (d) GG' (see Fig. 1 for the location of the cross sections). Dashed lines are plotted for $u = U$ and $u = 0$ ($U = 10$ m s^{-1}).

breaking and a pair of rotors, but the second rotor is smaller in amplitude. On the other hand, an additional experiment with $Nh_0/U = 0.6$ shows neither wave breaking nor rotor formation. The flow pattern obtained in this case is similar to that displayed in Fig. 3a except for a larger wave amplitude.

Since the vertical model resolution in the lowermost kilometer above ground is not particularly high (80 m on average), the question might arise whether the rotor and the boundary layer processes leading to its formation are adequately resolved in the model. Thus, a sensitivity test with 10 additional model levels in the relevant height range was conducted. The lowermost half-sigma level is located 12 m above ground in this test run. The results still exhibited a pair of rotors, but their horizontal extent was smaller than in the N2lf case shown in Figs. 12 and 13 because of an upstream shift of the flow separation point. Additional tests revealed that the location of the flow separation point depends somewhat on the distance of the lowermost model level from the ground. As it turned out, a reduction of the roughness length from 1 cm to about 0.7 cm would be needed to approximately reproduce the N2lf result with the higher vertical resolution. This indicates that the rotor formation is a reproducible feature, but the range of roughness lengths supporting rotor formation seems to depend on model details such as the vertical resolution or the boundary layer parameterization.

4. Summary and conclusions

This study investigates the airflow over a mountain ridge with a nondimensional half-width Na/U of about 1. Such a mountain induces a gravity wave spectrum, which is only partly able to propagate vertically. The impact of a level gap embedded in the mountain ridge

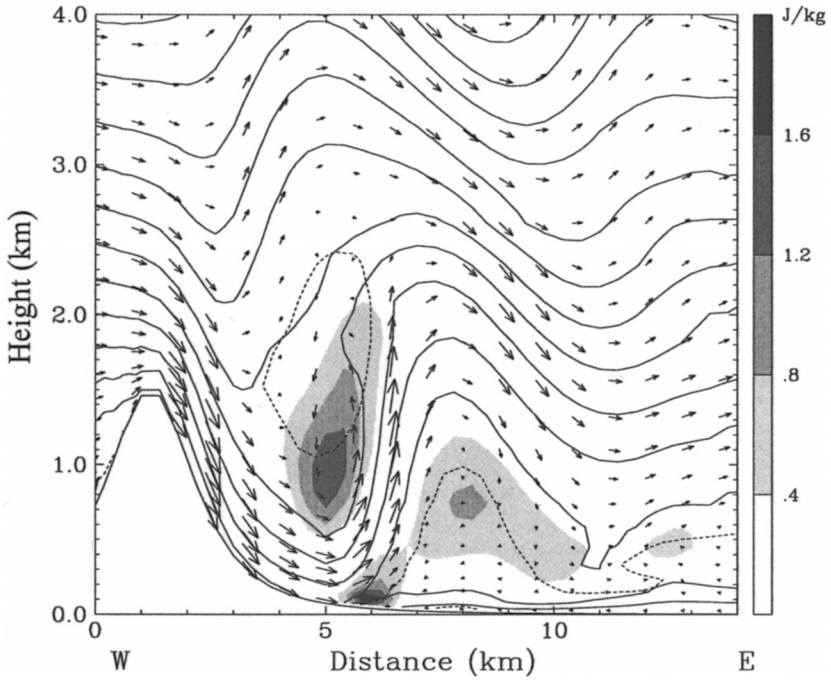

FIG. 13. Vertical cross section along line SR' (see Fig. 1) for simulation N2lf (Nh_0/U = 1.5, roughness length 1 cm). Solid lines denote potential temperature (contour interval 1K), shading denotes the turbulent kinetic energy predicted by the model's boundary layer parameterization (shading steps every 0.4 J kg^{-1}; see label bar). Wind vectors are scaled according to the aspect ratio of the figure; the maximum horizontal (vertical) speed is 17.1 m s^{-1} (8.3 m s^{-1}). The dashed line denotes $u = 0$.

is also examined. The standard setup of the numerical simulations uses a free-slip lower boundary condition and neglects the Coriolis force, but sensitivity experiments with surface friction and Coriolis force are also performed. A wide range of mountain heights is considered so as to assess the effect of nonlinearity on the flow behavior. Part of the results is compared with simulations for a wide mountain ridge reported previously (Zängl 2002b). Except for a much larger mountain width, these simulations were performed with the same model setup as those presented in this study.

In accordance with linear analytical solutions, the simulations with low mountains show that the parameter Na/U to a large extent controls the structure of the gravity waves and the concomitant wind perturbations. While a single surface wind maximum is located on the lee side of the mountain for $Na/U \gg 1$, an additional wind maximum at the mountaintop appears as Na/U approaches 1. With decreasing Na/U, the mountaintop wind maximum intensifies while the leeside wind maximum gradually disappears. Simultaneously, the gravity wave activity above the mountain weakens since an increasing part of the gravity wave spectrum excited by the mountain decays with height, and the pressure drag exerted by the mountain decreases. The simulations show that the ratio between the two surface wind maxima changes quite rapidly with Na/U in the parameter range of $Na/U \approx 1$. A decrease of Na/U by a factor of 1.5 increases the ratio between the wind perturbations at the peak and in the lee by a factor of 2.5. Moreover, it is found that the scaling of the wind perturbations predicted by the analytical solutions for the hydrostatic and the nonhydrostatic limit is still valid for $Na/U \approx 1$. For fixed Na/U, the wind perturbation at the mountain top is proportional to h_0/a, and the leeside wind perturbation still scales with Nh_0/U.

As nonlinear effects come into play, several aspects of the flow over a narrow mountain ridge change fundamentally. Most importantly, there is a range of mountain heights for which gravity wave breaking extends the hydrostatic flow regime with a pronounced leeside wind maximum close to a nondimensional half-width of 1. This effect is strongest for $Nh_0/U \approx 1$ and still present for $Nh_0/U = 1.5$. For higher mountains, however, flow separation from the ground occurs over the lee slope and shifts the surface wind pattern back to nonhydrostatic, the wind maximum again being at the mountain peak. A further decrease of Na/U below 1 prevents gravity wave breaking for any mountain height. As a consequence, the nonlinear wind amplification typical for wider mountains is absent. The maximum wind perturbation increases roughly linearly with mountain height up to some saturation value related to the onset of upstream blocking. Moreover, flow separation from the ground commences at much lower mountain heights than for wider mountains, and the wind maximum oc-

curs at the mountain crest regardless of the mountain height.

The wind perturbations found along the gap axis are qualitatively similar to those above the mountain ridge in that there is a wind minimum on the upstream side of the gap and a wind maximum in the lee. However, the tendency for the formation of a wind maximum at the gap center is weaker than for a wind maximum at the crest of a mountain ridge. Moreover, in the linear parameter range, the magnitude of the wind perturbations along the gap axis is rather weak. In this case, the pressure and wind perturbations along the gap axis are related to the three-dimensional propagation properties of gravity waves. When the adjacent mountain ridges are high enough to induce gravity wave breaking, the maximum wind speed along the gap axis becomes comparable to or even higher than that over the mountain ridge. The primary dynamical mechanism governing the gap flow in this case appears to be the cross-mountain pressure difference built up by the flow over the adjacent ridges. A hydraulic-like conversion of potential into kinetic energy may further enhance the wind speed on the lee side of the gap. The range of mountain widths and mountain heights for which nonlinear effects lead to a quasi-hydrostatic flow pattern with a single wind maximum in the lee is larger for gaps than for the adjacent mountain ridges.

In agreement with previous studies, surface friction is found to reduce the wind speed close to the ground, to promote flow separation from the ground and to reduce the tendency toward gravity wave breaking. For the simulations performed in this study, a roughness length of 50 cm completely suppresses wave breaking while a value around 1 cm still allows for wave breaking. An interesting aspect of these simulations is that the formation of rotors is possible not only in an environment that supports linear trapped lee waves, as is commonly believed. When the mountain is narrow enough for nonhydrostatic effects to be relevant, rotors may even form in the presence of a uniform large-scale flow.

Acknowledgments. I would like to thank Matthias Hornsteiner for the interesting discussions triggering this work. Moreover, I am grateful to the anonymous reviewers for their insightful comments that improved the paper significantly.

REFERENCES

Arakawa, S., 1969: Climatological and dynamical studies on the local strong winds, mainly in Hokkaido, Japan. *Geophys. Mag.,* **34,** 349–425.

Bacmeister, J. T., and M. R. Schoeberl, 1989: Breakdown of vertically propagating two-dimensional gravity waves forced by orography. *J. Atmos. Sci.,* **46,** 2109–2134.

Ballard, S. P., B. W. Golding, and R. N. B. Smith, 1991: Mesoscale model experimental forecasts of the Haar of northeast Scotland. *Mon. Wea. Rev.,* **119,** 2107–2123.

Bauer, M. H., G. J. Mayr, I. Vergeiner, and H. Pichler, 2000: Strongly nonlinear flow over and around a three-dimensional mountain as a function of the horizontal aspect ratio. *J. Atmos. Sci.,* **57,** 3971–3991.

Clark, T. L., and W. R. Peltier, 1977: On the evolution and stability of finite-amplitude mountain waves. *J. Atmos. Sci.,* **34,** 1715–1730.

Doyle, J. D., and D. R. Durran, 2002: The dynamics of mountain-wave-induced rotors. *J. Atmos. Sci.,* **59,** 186–201.

Drobinski, P., J. Dusek, and C. Flamant, 2001: Diagnostics of hydraulic jump and gap flow in stratified flows over topography. *Bound.-Layer Meteor.,* **98,** 475–495.

Dudhia, J., 1993: A nonhydrostatic version of the Penn State/NCAR Mesoscale Model: Validation tests and simulations of an Atlantic cyclone and cold front. *Mon. Wea. Rev.,* **121,** 1493–1513.

Durran, D. R., and J. B. Klemp, 1982: The effects of moisture on trapped mountain lee waves. *J. Atmos. Sci.,* **39,** 2490–2506.

Flamant, C., and Coauthors, 2002: Gap flow in an Alpine valley during a shallow south föhn event: Observations, numerical simulations and hydraulic analogue. *Quart. J. Roy. Meteor. Soc.,* **128,** 1173–1210.

Gayno, G. A., 1994: Development of a higher-order, fog-producing boundary layer model suitable for use in numerical weather prediction. M.S. thesis, Dept. of Meteorology, The Pennsylvania State University, 104 pp. [Available from Dept. of Meteorology, The Pennsylvania State University, University Park, PA 16802.]

Georgelin, M., E. Richard, M. Petitdidier, and A. Druilhet, 1994: Impact of subgrid-scale orography parameterization on the simulation of orographic flows. *Mon. Wea. Rev.,* **122,** 1509–1522.

Grell, G. A., J. Dudhia, and D. R. Stauffer, 1995: A description of the fifth-generation Penn State/NCAR mesoscale model (MM5). NCAR Tech. Note NCAR/TN-398+STR, 122 pp.

Klemp, J. B., and D. R. Durran, 1983: An upper boundary condition permitting internal gravity wave radiation in numerical mesoscale models. *Mon. Wea. Rev.,* **111,** 430–444.

Koffi, E. N., M. Georgelin, B. Benech, and E. Richard, 2000: Trapped lee waves observed during PYREX by constant volume balloons: Comparison with Meso-NH simulations. *J. Atmos. Sci.,* **57,** 2007–2021.

Olafsson, H., and P. Bougeault, 1996: Nonlinear flow past an elliptic mountain ridge. *J. Atmos. Sci.,* **53,** 2465–2489.

——, and ——, 1997: The effect of rotation and surface friction on orographic drag. *J. Atmos. Sci.,* **54,** 193–210.

Peltier, W. R., and T. L. Clark, 1979: The evolution and stability of finite-amplitude mountain waves. Part II: Surface wave drag and severe downslope windstorms. *J. Atmos. Sci.,* **36,** 1498–1529.

Phillips, D. S., 1984: Analytical surface pressure and drag for linear hydrostatic flow over three-dimensional elliptical mountains. *J. Atmos. Sci.,* **41,** 1073–1084.

Queney, P., 1948: The problem of airflow over mountains: A summary of theoretical studies. *Bull. Amer. Meteor. Soc.,* **29,** 16–26.

Richard, E., P. Mascart, and E. C. Nickerson, 1989: The role of surface friction in downslope windstorms. *J. Appl. Meteor.,* **28,** 241–251.

——, ——, and ——, 1990: Examples of the role of surface friction in downslope windstorms. *Meteor. Atmos. Phys.,* **43,** 163–172.

Sawyer, J. S., 1960: Numerical calculations of the displacements of a stratified airstream crossing a ridge of small height. *Quart. J. Roy. Meteor. Soc.,* **86,** 326–345.

Scorer, R. S., 1949: Theory of waves in the lee of mountains. *Quart. J. Roy. Meteor. Soc.,* **75,** 41–56.

Shutts, G., 1992: Observations and numerical model simulation of a partially trapped lee wave over the Welsh mountains. *Mon. Wea. Rev.,* **120,** 2056–2066.

Sládkovič, R., and H.-J. Kanter, 1977: Low-level jet in the Bavarian pre-Alpine region. *Arch. Meteor. Geophys. Bioklimatol.,* **25A,** 343–355.

Smith, R. B., 1979: The influence of mountains on the atmosphere. *Advances in Geophysics,* Vol. 21, Academic Press, 87–229.

——, 1980: Linear theory of stratified hydrostatic flow past an isolated mountain. *Tellus*, **32,** 348–364.

Stein, J., 1992: Investigation of the regime diagram of hydrostatic flow over a mountain with a primitive equation model. Part I: Two-dimensional flows. *Mon. Wea. Rev.*, **120,** 2962–2976.

Vosper, S. B., S. D. Mobbs, and B. A. Gardiner, 2002: Measurements of near-surface flow over a hill. *Quart. J. Roy. Meteor. Soc.*, **128,** 2257–2280.

Xue, M., and A. J. Thorpe, 1991: A mesoscale numerical model using the nonhydrostatic pressure-based sigma-coordinate equations: Model experiments with dry mountain flows. *Mon. Wea. Rev.*, **119,** 1168–1185.

Zängl, G., 2002a: An improved method for computing horizontal diffusion in a sigma-coordinate model and its application to simulations over mountainous topography. *Mon. Wea. Rev.*, **130,** 1423–1432.

——, 2002b: Stratified flow over a mountain with a gap: Linear theory and numerical simulations. *Quart. J. Roy. Meteor. Soc.*, **128,** 927–949.